Schedule for Presentation Meeting of Master-Degree Thesis in 2017
International Course of Maritime & Urban Engineering

Date :   August 2nd (Wednesday) starting from 10:00
Venue :   S1-312   Lecture Room

No.	Time	Name	Supervisor	Title of thesis	Chairman
1	10:00 – 10:25	Hossain MD. Alfaz	Toda	Force, Motion and Nominal Wake Prediction for KCS Model with Heave and Pitch Free Condition in Head Waves	Aoki
2	10:25 – 10:50	Ma Jianping	Kashiwagi	Study on the Cloaking Phenomenon in Shallow Water Waves by Designing the Geometry of Seabed	Aoki
3	10:50 – 11:15	Silva Kukulege Bhathisha Akalanka	Araki	Role of Beach Morphology in a Tsunami Event - A Numerical Case Study Based on 2004 and 2011 Tsunami Disasters	Aoki
4	11:15 – 11:40	Su Sandy Htun	Umeda	Water-on-Deck Effects on Roll Motions of an Offshore Supply Vessel in Regular Stern Quartering Waves	Aoki
				Lunch Break	
5	13:15 – 13:40	Sumanto Nugroho	Kita	A Study on Socio-spatial Structure of Informal Settlements by Analyzing Relationships between Physical Environment and Human Behaviors in the Inner-city Kampung, Jakarta	Fujikubo
6	13:40 – 14:05	Htike Aung Kyaw	Toda	Flow Field Measurement Around Self-Propelled KRISO Container Ship Model in Head Waves	Fujikubo
7	14:05 – 14:30	Ahmad Zakky	Osawa	Numerical Study on Determination Technique for Equivalent Distributed Stress	Fujikubo
				Break	
	14:45 –	at S1-323 Meeting for Evaluating Mater-thesis Presentations, and Steering Committee Meeting			

Meeting for Evaluation: From 14:45 at S1-323 Meeting Room
                          Members are Steering committee members and the supervisors

Force, Motions and Nominal Wake Prediction for KCS Model with Heave and Pitch Free Conditions in Head Waves

Md Alfaz Hossain

Hull Form Design Sub-Area, Department of Naval Architecture and Ocean Engineering

Key Words: *CFD, Ship Motions, Added Resistance, Nominal Wake, Head Waves*

1. Introduction

The prediction of ship motions and added resistance is very important for safe and economic operation of the ship. Fuel consumption of a ship is strongly related to the ship motions and added resistance. The wake profile and behavior has influence on the propeller performance and hence on the fuel consumption as well. The Marine Environment Protection Committee (MEPC) of International Maritime Organization's (IMO) has imposed regulations for seagoing ships to maintain a minimum energy efficiency level, which is determined by Energy Efficiency Design Index (EEDI) and Energy Efficiency Operational Indicator (EEOI). Therefore, it is of vital importance to make a reliable prediction of ship motions, added resistance and nominal wake to meet criteria of EEDI and EEOI.

2. Methodology

CFD has been used to predict the force, motions and nominal wake of the KRISO Container Ship (KCS) model (without propeller) for Froude number 0.261, with heave and pitch free conditions, in calm water and in regular head wave conditions, recommended by CFD workshop 2015. The length between perpendiculars (L_{PP}) of the model ship is 3.2m for which PIV measurements have also been carried out at Osaka University.

The grid was generated using Gridgen. Then SUGGAR library was used for the overset of grids. CFDShip-IOWA V4.5 (which is an overset, block structured, and incompressible URANS code coupling with motion solver) has been used for numerical prediction. The k-ω SST turbulence model was employed using no wall function. A single-phase level-set method has been used to model the free surface and 2DOF (heave and pitch) ship motions are considered. The computational domain and boundary condition is shown in Fig. 1.
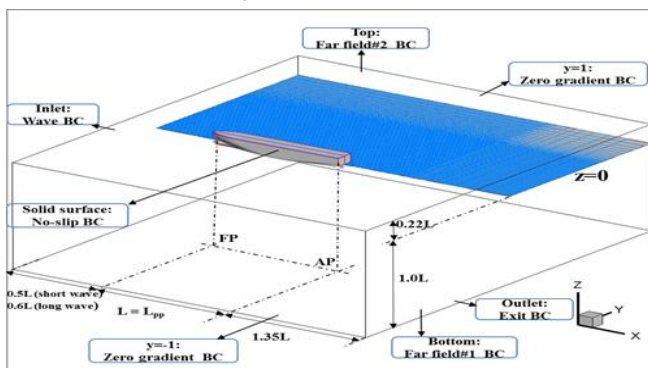

Fig. 1 Computational domain and boundary conditions.

3. Results

3.1 Ship motions and added resistance

CFD and EFD results of heave motion amplitude (z/A), pitch motion amplitude (θ/Ak), and added resistance(σ_{AW}), shown in

Fig. 2-4 respectively, made good agreement on the trend. In short waves, typically λ/L<0.5, z/A and θ/Ak are near zero indicating small vertical motions and corresponding lower σ_{AW} due to wave diffraction hitting the ship bow. With the increase of λ/L, vertical motions increase and consequently σ_{AW} increases until it reach to the peak value at λ/L=1.15 (wave resonance condition). In long waves, especially λ/L>1.15, z/A and θ/Ak both are close to one which indicates the ship moves up vertically as the wave amplitude and the pitch angle follows the wave slope. As a result, σ_{AW} drops down.
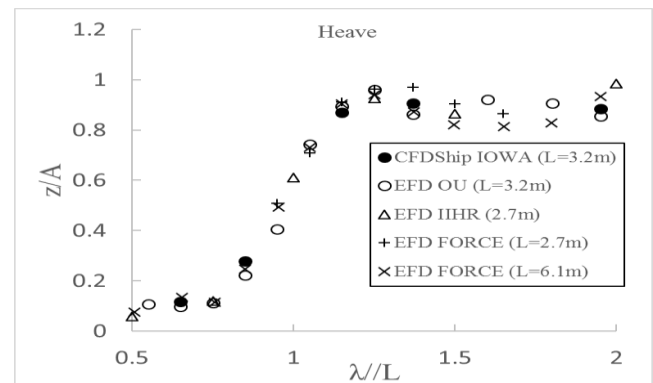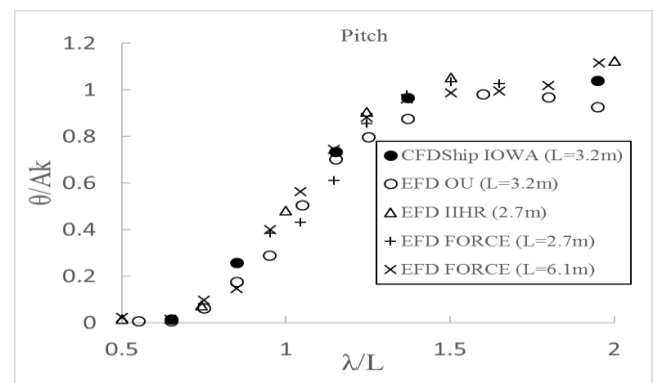

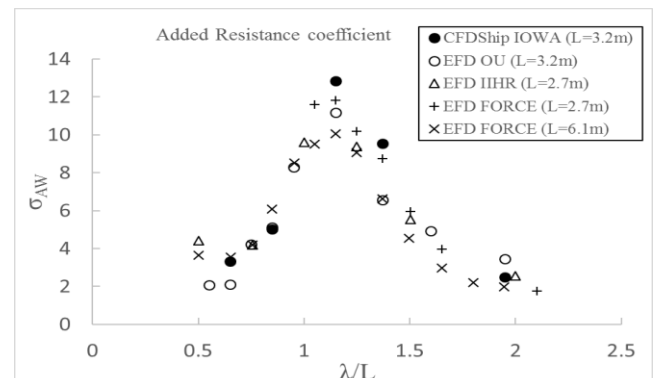Fig. 2 Heave motion amplitude.

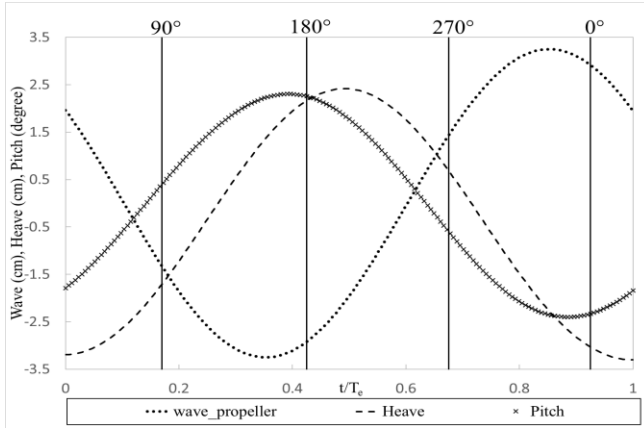Fig. 3 Pitch motion amplitude.

Fig. 4 Added resistance coefficient.

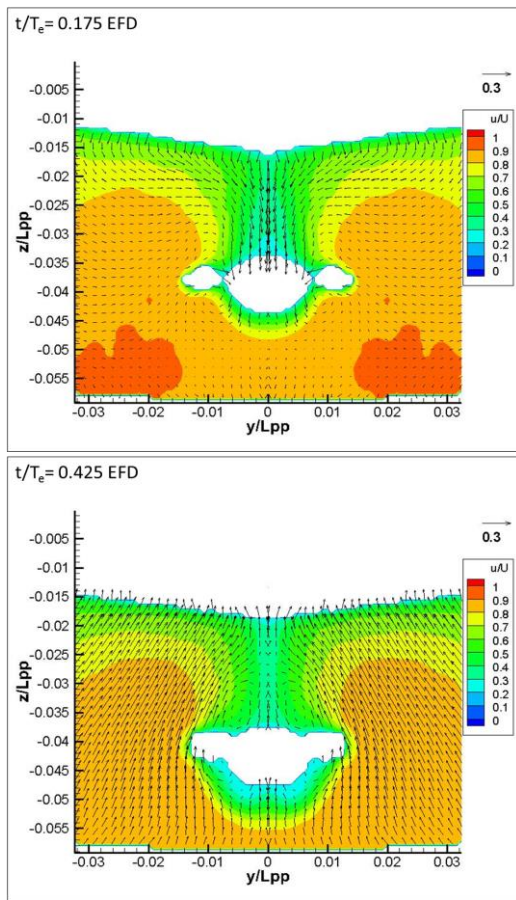Fig. 5 One period of wave at propeller plane, heave and pitch motions (CFD results) for λ/L=1.15.

the dummy boss although the secondary vortex is suppressed under the boss. When t/T_e = 0.425, the ship stern starts to move upward and thus the low speed area under the boss outspreads downward. The secondary vortex is clearly noticeable this time. The bilge vortex is found just above the boss.

4. Conclusions

The predicted motions and added resistance show very good agreement with EFD data which reveals that the CFDShip-IOWA solver is good enough to make reliable prediction for high-speed vessels. In addition, the CFD wake field at propeller plane shows very good agreement with PIV measurement.

For future work, propeller will be included for more realistic prediction and vortex behavior at the propeller plane will be analyzed in details as well.

Fig. 6 Nominal wake velocity at the propeller plane (PIV).
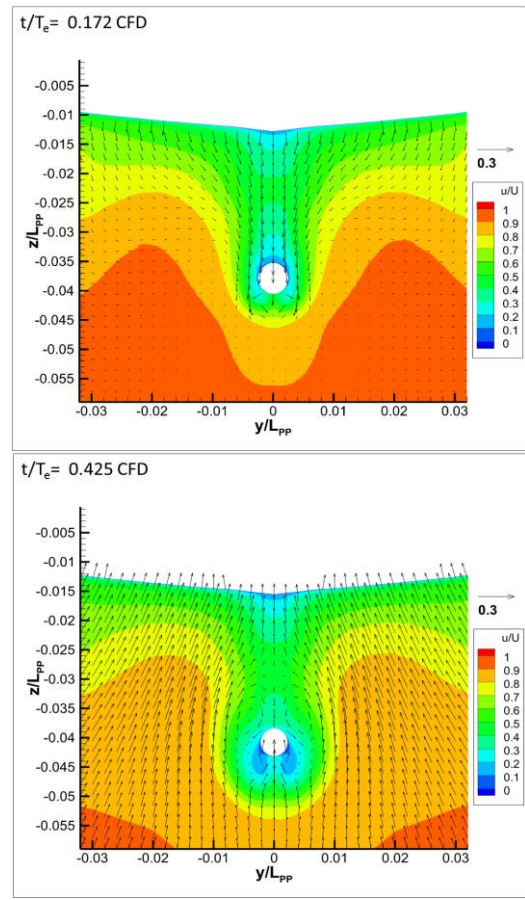
Fig. 7 Nominal wake velocity at the propeller plane (CFD).

3.2 Nominal wake

The comparison between CFD and EFD (PIV) results of nominal wake velocity at propeller plane has been done for λ/L=0.65, 1.15 and 1.37 for one-quarter of period (T_e). Four time instances (t/T_e), for λ/L= 1.15, are shown in Fig. 5 with vertical lines. 0°, 90°, 180° and 270° are the wave phases at the wave gauge measured during PIV experiment. Results for only λ/L=1.15 at two time instances have been shown in Fig. 6-7. t/T_e =0, when the wave crest is at bow (FP). When t/T_e~0.17, the ship stern goes downward which can be easily understood by the low speed area (in blue color shedding) above the dummy boss. The bilge vortex can be observed on the sides of dummy boss.

References

1) Hosseini, H., P. Wu, P. Carrica, H. Kim, Y. Toda, F. Stern: J of Ocean Engineering, Vol. 59, pp. 240–273, 2013.
2) Wu, P., H. Sadat-Hosseini, F. Stern, Y. Toda: J of JASNAOE, Vol. 24, pp. 13-19, 2017.
3) Wu, P., E. Tokgoz, H. Okawa, K. Tamaki, Y. Toda: Computational and Experiment of Propeller Performance and Flow Field around Self-propelled Model Ship in Regular Head Waves, Proc. of 31st SNH (California, USA), 2016.
4) http://www.t2015.nmri.go.jp/Instructions_KCS/Case_2.10/Case_2-10.html

Study on the Cloaking Phenomenon in Shallow Water Waves by Designing the Geometry of Seabed

Ma Jianping

Ocean Space Development Subarea, Department of Naval Architecture and Ocean Engineering

1. Introduction

In recent years, inspired by the pioneering idea of Pendry, Schurig & Smith[1], there are plenty of work concentrating on the study of cloaking by constructing specific metamaterials in different research fields, such as electromagnetic waves and acoustic waves. The core concept of this sort of cloaking is to shield objects by utilizing a coordinate transformation method to design the material parameters, which can steer the waves in any desired trajectory. Zareei & Alam[2] extended the cloaking into shallow water wave field by applying a nonlinear transformation that requires a spatially variable water depth.

Based on the previous research, this paper presents a rigorous derivation of the water depth tensors for both the rectangle and cylinder shaped cloaks. The analytical solution and the implementation of water depth tensor for cylindrical cloaking are also studied. In addition, the distribution of plane wave and cylindrical wave cloaking are simulated. In this study, a linear potential flow is assumed and FEM-based commercial software COMSOL Multiphysics is employed for numerical computations.

2. Governing Equation

Assuming the waves to be sinusoidal in time with radian frequency ω, the governing equation for the propagation of long waves (i.e. $kh \ll 1$, where k, $h = h(x)$ are the wavenumber and water depth respectively) is the shallow water equation, which is written as

$$\nabla \cdot (h \nabla \eta) + \frac{\omega^2}{g} \eta = 0 . \tag{1}$$

Here g denotes the gravitational acceleration and η means the wave elevation. A very important property of the shallow water equation is form-invariant, therefore it will keep the same form in any arbitrary coordinate system. In a new coordinate, keeping the g as the real world gravitational acceleration, water depth is given by

$$\bar{h} = F G_O^{-1} F^T G_P h , \tag{2}$$

where F is the Jacobian of transformation, and G_O and G_P represent metric tensor of original and transformed physical coordinates, respectively.

3. Coordinate Transformation

3.1 Cylindrical Cloak

In order to achieve the cylindrical cloak, the following nonlinear transformation is taken into account

$$\begin{cases} r_p = \sqrt{(1 - \frac{a^2}{b^2}) r_o^2 + a^2} \\ \theta_p = \theta_o \end{cases} \tag{3}$$

where a and b are radii of inner and outer cloaking domains. Then the coordinate system is distorted as shown in Fig.1. Applying this transformation into (2) yields the water depth tensor expressed as

$$\bar{h} = \left(1 - \frac{a^2}{b^2}\right) \begin{pmatrix} \dfrac{r_p^2 - a^2}{r_p^2} & 0 \\ 0 & \dfrac{r_p^2}{r_p^2 - a^2} \end{pmatrix} h . \tag{4}$$
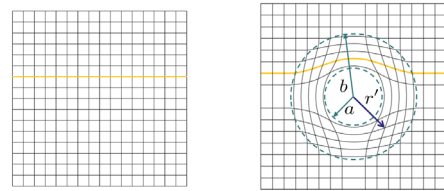

Fig. 1   Coordinate transformation for cylindrical cloak.

3.2 Square Cloak

The same idea as the cylindrical cloak can be used for design of a square-shaped cloak with inner square width 2a and outer square width 2b. It can be seen that the coordinate transformation

$$\begin{cases} x_p = \sqrt{(1 - \frac{a^2}{b^2}) x_o^2 + a^2} , \\ y_p = \dfrac{\sqrt{(1 - \frac{a^2}{b^2}) x_o^2 + a^2}}{x_o} y_o . \end{cases} \tag{5}$$

mapped the right triangle in the original space into the right subdomain in the transformed physical space (as Fig. 2). Consequently the equivalent water depth tensor is obtained

$$\bar{h} = \begin{pmatrix} (1 - \frac{a^2}{b^2})^2 \dfrac{x_o^2}{x_p^2} & -(1 - \frac{a^2}{b^2})^2 \dfrac{a^2}{x_o x_p^2} y_o \\ -(1 - \frac{a^2}{b^2})^2 \dfrac{a^2}{x_o x_p^2} y_o & \dfrac{a^4}{x_o^4 x_p^2} y_o^2 + \dfrac{x_p^2}{x_o^2} \end{pmatrix} h . \tag{6}$$

The corresponding formulas for upper, left and bottom subdomains can be similarly obtained by applying rotation operators with rotation angles of π/2, π and 3π/2.
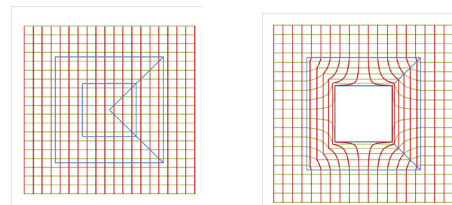

Fig. 2   Coordinate transformation for square cloak.

4. Cloaking Factor

For the purpose of measuring the efficiency of cloaking, we are

supposed to calculate the cloaking factor, which means the ratio of the total energy scattered by the object in the existence of the cloak to the total energy scattered when seabed is flat, and it is defined by Porter & Newman [3] as

$$\Omega = \frac{\sigma_{clk}}{\sigma_{flt}}. \tag{7}$$

As can be seen from Fig.3, with the increase of ratio b/a, the cloaking factor can decrease to almost zero, a perfect cloaking.
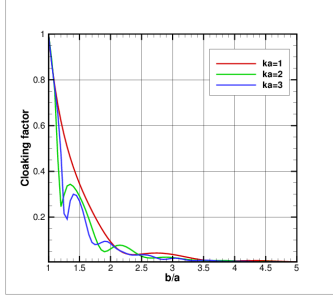

Fig. 3   Cloaking factor for the nonlinear mapping against cloak size b/a with different value of ka.

5.   Homogenization Theory

For the sake of realizing the anisotropic water depth described in (4), we should apply the homogenization theory to design the equivalent topography of seabed. Considering a two-layered system, and each layer ought to be homogenous and isotropic. Here we let the water depth $h = h(r)$ varies in the radial direction between constant water depth h_1 and h_2 with the same width. According to the homogenization theory, we obtain

$$h_1(r_p) = h_\theta[1 + (1 - \frac{h_r}{h_\theta})^{1/2}],$$

$$h_2(r_p) = h_\theta[1 - (1 - \frac{h_r}{h_\theta})^{1/2}]. \tag{8}$$

Keeping it in mind, we give an example for the geometry of water depth consisting of 10 layers as shown in Fig. 4.
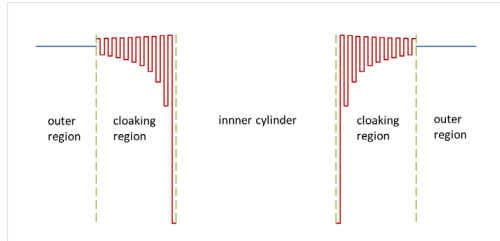

Fig. 4 Cross-sectional view of multi-layered water depth structure.

6.   Discussions and Conclusions

The results of numerical computations are demonstrated as Fig. 5-8. It is seen that the cloaking effect of cylinder-shaped cloak is asymptotically perfect for both plane waves and cylindrical waves. Concerning the square-shaped cloak, to some extent, it can perform well. However it is not good as the cylindrical cloak, overall. The imperfection may be attributed to the unsmoothed coordinate after transformation.

Here we show a scheme of designing a cloak for shallow water waves via coordinate transformation method. Compared to some other techniques to realize the cloaking, this type of cloaking has a number of advantages. For instance, the presented cloak is omnidirectional and effective for all frequency water waves as long as it is under the assumption of shallow water wave. Meanwhile, there are some drawbacks needed to be overcome. For the seabed topography exhibited in Fig. 4, sedimentation or erosion will soon make the cloak ineffective. Therefore, these issues are expected to be solved appropriately in the future.

Fig. 5   Water pattern of cylinder-shaped cloaking for plane wave.
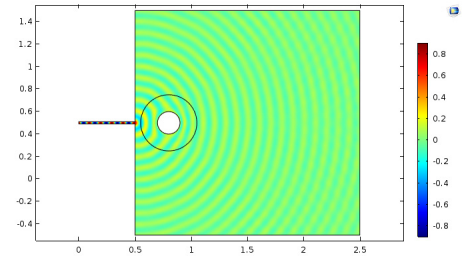
Fig. 6   Water pattern of cylinder-shaped cloaking for cylindrical wave.

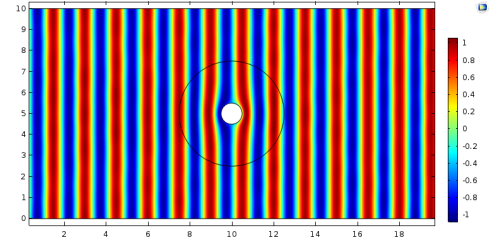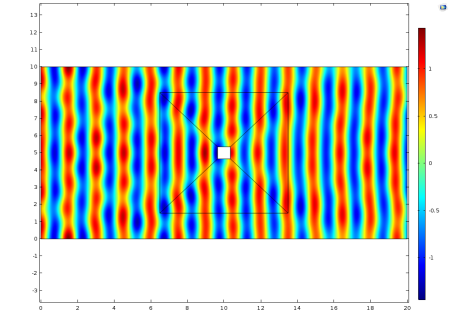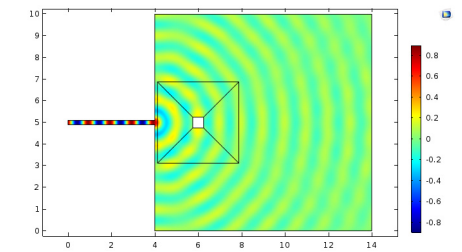Fig. 7   Water pattern of square-shaped cloaking for plane wave.

Fig. 8   Water pattern of square-shaped cloaking for cylindrical wave.

References

1） Pendry, J. B., Schurig, D., & Smith, D. R.: SCIENCE, Vol.312, No.5781, pp.1780-1782, 2006.
2） Zareei, A. & Alam, M.-R.: J. Fluid Mech, Vol.778, pp. 273-287, 2015.
3） Porter, R. & Newman, J. N.: J. Fluid Mech, Vol.750, pp.124-143, 2014.

Role of Beach Morphology in a Tsunami Event – A Numerical Case Study Based on 2004 and 2011 Tsunami Disasters

Akalanka Silva

Land Development and Management Engineering Laboratory, Department of Civil Engineering

Key Words: *Tsunami, Beach Morphology, Inundation, Delft3D Flow, SWAN*

1. Introduction

Tsunami is a series of ocean waves that occur often due to submarine earthquakes. These gigantic waves sends surges of water, sometimes reaching heights of over 30 meters on to land. These wave trains can cause widespread destruction with in a very short time frame when they strike ashore. Once generated, tsunamis race across the sea at up to 800 kilometers per an hour. And their long wavelengths mean they lose very little energy along the way. When it reaches shallow water, celerity will drop and water will build up to several meters due to shoaling effect, keeping energy conservation. When buildup reaches a critical level, wave breaks or inundates as a surging front depending on the bed slope and other morphological features of the coast line. A tsunami can run up to several miles on a flat land or an unprotected beach until it dissipate its energy.

1.1 Focus and Objectives

When a tsunami strikes, the damage it would cause is not only depend on wave energy but also on morphological features of the coastline. Disasters occurred in recent times left important evidences that proves above fact as some affected areas were totally destroyed while some showed very less damage. Therefore, having an idea on this nature is important. The primary aim of the study is to identify the common morphological features of coastal areas of which a tsunami will destructively impact. Objectives are achieved by a numerical recreation of 2004 and 2011 events.

2. Methodology

2.1 Literature Review and Data Collection

The energy dissipation of tsunami and wind wave are different due to the characteristics of the two kinds of waves. Tsunami is a shallow water wave, even in Deep Ocean, with very long wavelength and relatively high especially near shore. It does not break when attacking the shore rather composed of run-up and run-down[1]. From this fact, and as coastal morphology directly governs wind wave energy dissipation, it could be suggested that the role of beach morphology in a tsunami event is different than the behavior ahead of wind waves.

To assess the role, various data was collected focusing 2004 and 2011 tsunami events. Bathymetry data was extracted from freely available GEBCO data set. Earthquake parameters were acquired from USGS online data base and water level observations of 2011 tsunami in several locations were downloaded from NOWPHAS.

2.2 Bathymetry Preparation and Tsunami Generation

Firstly, two main regional domains were made to cover the area of 2004 and 2011 tsunamis. WGS84 spherical coordinate system was used and bathymetries were fitted in to rectangular grids having resolution of 0.02^0 (approximately 1.7 x 2.2 km). Initial displacements were calculated accounting USGS earthquake parameters by Okada's equations[2]. Up to this point calculations were done in Matlab environment.

2.3 Tsunami Propagation

Wave propagation was simulated via Delft3D Flow module applying water surface deformation resulted from earthquakes as initial conditions (Fig. 1). Delft3D Flow is a multi-dimensional hydrodynamic simulation program. The flow module is based on shallow water equations with bossinesq approximation applied (Equation 1 and 2)[3].

$$\partial_t U + \nabla_H \left(\frac{U^2}{h} \right) + fkU =$$

$$-gh\nabla_H(h - H) + \rho_o^{-1}(\tau_s - \tau_b) + X \qquad (1)$$

$$\partial_t h + \nabla_H U = 0 \qquad (2)$$

$$\text{Where } U = \int_{-H}^{\eta} u\,dz$$

η is surface deviation, H is equilibrium depth, $f = 2\Omega sin\phi$, Ω is Earth's rotation rate, ϕ is latitude, ρ_0 is reference density, $h = \eta + H$, u is velocity vector in x, τ_s, τ_b are turbulent vertical momentum fluxes at top and bottom, X denotes integrated horizontal momentum fluxes.
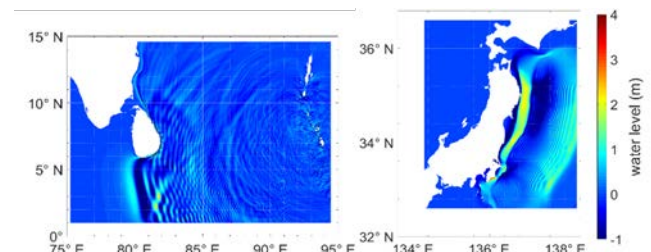
Fig. 1 Simulations of 2004 and 2011 tsunami events.
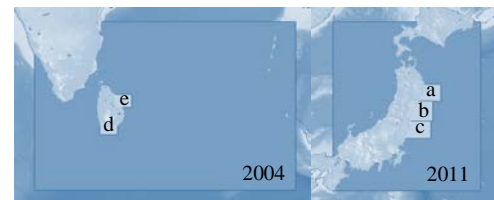
Fig. 2 Distribution of local models inside main domains.

2.3 Coastal Interaction

Five separate local domains were built in higher resolution of 0.002^0 (approximately 170 x 220 m) inside main two domains (Fig. 2) to assess the coastal interaction of the upcoming tsunami. Wave conditions extracted from calibrated regional models were fed in to local models from open boundaries as time series.

2.4 Assessment of Some Common Features in a Coastline

In addition to local domains mentioned above, a common bathymetry was prepared that consists of general morphological

features to further investigate the behavior of tsunami striking on a bay and headlands (Fig. 3). This is inspired by the results of above mentioned simulations.

Fig. 3 Common bathymetry with focus points.

2.5 Assessment of Wind Wave vs Tsunami

The common domain is then subjected to an irregular wind wave condition ($H_s=1m$, $T_p=6s$, *Wind speed=10m/s from East*) to investigate the differences of energy dissipation compared to tsunami. Wind wave field is calculated via SWAN. SWAN is a fully spectral third generation wave model which is based on the discrete spectral action balance equation. It also uses fully implicit schemes thus become unconditionally stable.

3. Results and Discussion

3.1 Results of Regional Models

Tsunami propagation from source to shallow water is focused in regional model stage. Calibration is done by comparing water level variations at numerous locations of 2011 Japan tsunami event with measured data. Figure 4 shows the calibration plot at Southern Iwate (N$39^0$15'31'' E$142^0$05'29'')
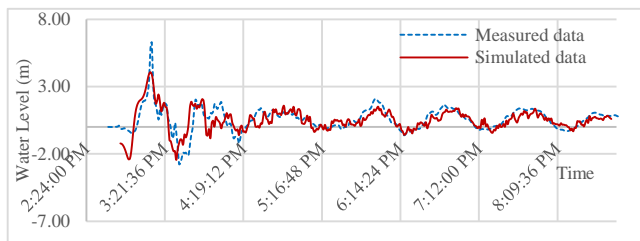
Fig.4 Comparison of measured and simulated data (2011 event).

3.1 Results of Local Models

Water level variations, Current velocities and bed shear stresses were extracted from each local model at numerous focus points. A sample focus area and parameter extraction points are illustrated in Figure 5. Figure 6 gives the comparison of water level variations at different focus points.
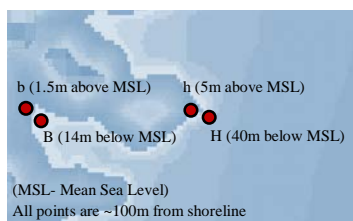
Fig. 5 A set of focus points of local model "a".

Both events in 2004 and 2011 acted similarly from the view point of coastal interaction. Water level heights, current velocities and bed stresses at partially closed bays showed significantly higher values than those in front of headlands or flat beaches.
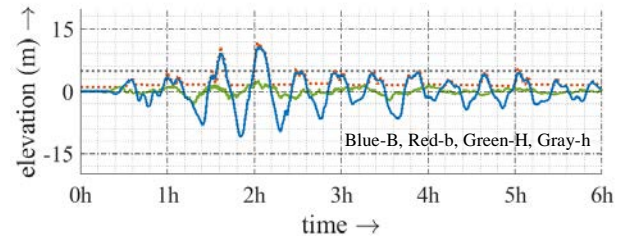
Fig. 6 Water level variations at one set of focus points.

3.2 Results of the Common Model

Hydrodynamic parameters explained above were extracted similarly from simulation of common domain. In addition to that wind wave field was extracted from the wave model and results are shown in Figures 7 and 8 respectively.
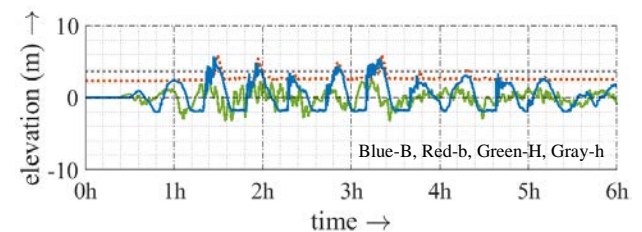
Fig. 7 Water level variations at focus points in common domain.

Fig 8. Wind wave field at steady state.

Alike behavior to local models that explained above was observed in tsunami simulation while wind wave is dissipating its energy in a conventional manner which is higher wave heights near headlands and comparatively lower energy concentration inside the bay.

4. Conclusions

The behavior of a tsunami at a coastline directly depend on beach morphology. The relation is comparatively different from that of wind waves as higher energy concentration observed in partially closed areas such as bays. Results and findings will be useful for planners and designers of tsunami protection measures in the future.

References

1) Pal, B. Panda, K. Comparison of erosional features by tsunami and wind waves, ICRAGEESD, San Diego, May 2010.
2) Okada, Y. Surface deformation due to shear and tensile faults in a half-space, Bulletin of SSA, Vol. 75, No. 4, pp.1135-1154, August 1985.
3) Dutykh, D. Mathematical modelling of tsunami waves, Mathematics Ecole normale superieure de Cachan - ENS Cachan, January 2008.

Water-on-Deck Effects on Roll Motions of an Offshore Supply Vessel in Regular Stern Quartering Waves

Su Sandy Htun

Ship Design Subarea, Department of Naval Architecture and Ocean Engineering

Key Words: offshore supply vessel, water on deck, pure loss of stability, roll damping, second generation intact stability criteria

1. Introduction

The second generation intact stability criteria are currently under development at the International Maritime Organization; (IMO). These criteria are physic-based, consisting of two-leveled vulnerability criteria and direct stability assessment. One of the remaining issues is the applicability of the criteria for preventing pure loss of stability in astern waves to offshore supply vessels (OSV). OSVs show an inconsistency problem in the first and second level criteria.

OSVs have extended low weather decks about half of the ship length which is surrounded by bulwarks with freeing ports. But they often have no bulwark at stern end because of operational purpose. Thus, in heavy seas, large amount of water can be trapped on the weather deck.

Dillingham[1] performed numerical simulation of 2D flow of water on deck (WOD) of a fishing vessel in beam seas and Falzarano et al[2] improved this method to apply to 3D flow of water on deck of an OSV in beam seas. Both approved by numerical simulation that the water on deck reduces the roll but not always. Umeda, Aqmil et al[3] performed a model experiment of an OSV in regular stern quartering waves and compared it with numerical model proposed by Kubo et al[4]. They found that there were no severe roll at high speed but there was the large heel at low speed. These results cannot be explained by the simulation which does not take into account of the water on deck.

In this research, the effect of low weather deck length and the effect of water on deck on the behavior of OSVs are investigated. Free running model experiments of the OSVs are performed with models having the same hull form but different low weather deck lengths. Also, the experiment results are compared with numerical simulation which considers the water on deck effect.

2. Model Experiment

2.1 Ship Model

The ship model used is the same one as in Umeda, Aqmil et al[3]. Principal particulars of the OSV are shown in Table 1. But, in the current experiment, the original model was modified into four different models based on low weather deck length and GM as shown in Table 2.

Table 1 Principal particulars of the OSV.

Length, L_{pp}	60.00m
Breadth, B	16.40mm
Depth, D	7.20m
Molded draught, d	6.00m
Metacentric height, GM	1.45m

The experiment was conducted for regular waves of two wave cases (the wavelength to ship length ratio, $\lambda/L = 1.0$, and the wave steepness, $H/\lambda = 0.1$, $\lambda/L = 1.5$ and $H/\lambda = 0.1$). The heading angle was 30 degrees from the wave direction and the tested Froude numbers range from 0.15 to 0.37.

Table 2 Length of low weather decks of the used models.

	Length of low weather deck, l	l/L_{pp}	GM
Original OSV	39.94 m	0.67	1.45m
Case 1	0 m	0.0	1.45m
Case 2	10.48 m	0.17	1.45m
Case 3	25.21 m	0.42	1.45m
Case 3 with reduced GM	25.21 m	0.42	1.053m

The cases of 1, 2, and 3 are also checked with the draft pure loss level 2 criteria. Case 1 and Case 2 pass the Level 2 but Case 3 fails. This indicates that model in Case 3 can be vulnerable to pure loss of stability according to the level 2 criteria.

2.2 Experiment Results

The results from model experiment for the wave case of $\lambda/L = 1.5$ and $H/\lambda = 0.1$ are shown in Fig. 1. For a comparison sake, the experiment result of original model[3] is also included.
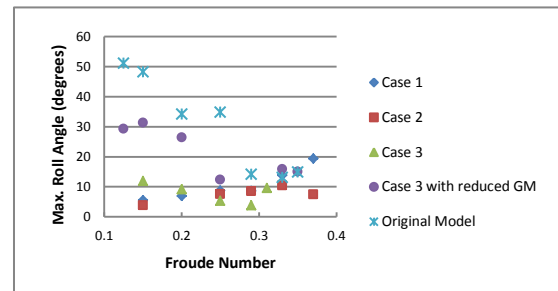
Fig. 1   Experimental results of all four model cases compared with original model result.

For Case 1, Case 2 and Case 3 models, the roll angles are not so large and also no tendency of pure loss of stability. However, as stated before, Case 3 is judged as vulnerable to pure loss by the level 2 criteria check. Thus, some contradictions exist between the level 2 criteria result and experiment result.

For Case 3 model with reduced GM, large roll angles are found for low speed (Fn<0.25). During the experiment, it was found that a large amount of water entered from the stern for this case and despite the egress through the freeing ports, the ingress from stern is much larger. Thus, this large roll angles can be considered due to the static heeling moment of large volume of water trapped on deck.

3. Numerical Simulation

3.1 Simulation model

Numerical simulation using a coupled surge-sway-yaw-roll model developed by Kubo[4] which is based on the maneuvering model for ships in calm water by Hirano and Takashima[5] is applied. The linear wave-induced forces and moments are calculated by slender body theory with low encounter frequency assumption, (Umeda[6]). The maneuvering coefficients were estimated empirically and the roll damping coefficient, the calm-water resistance and propeller open characteristics were obtained by model experiments.

3.2 Simulation Results

The simulation results for all model cases are shown in Fig. 2. Not so good agreement between experiment and simulation is found except for Case 1, (which has no low weather deck so that also no WOD).
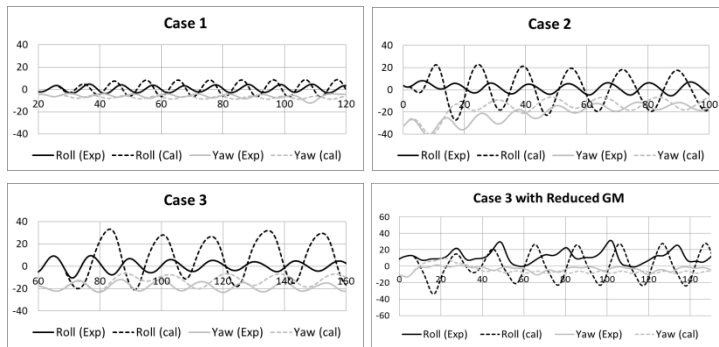
Fig. 2   An example of time series of each case in regular waves of λ/L=1.5 and H/λ=0.1. Here, the Froude number is 0.15 for Case 1, 0.29 for Case 2 and Case 3 and 0.15 for Case 3 with reduced GM.

3.3 Water on Deck

For Case 2 and Case 3, having low weather deck, a certain amount of water can enter and be trapped. If some phase lag exists between the natural roll frequency of trapped water and the ship roll frequency, the water on deck may act as anti-rolling device. Since the 4DOF model does not take into account of this, I attempt to use the ITTC recommended estimation formula[7] for the equivalent linear roll damping due to flooded water, which is based on the database obtained from a systematic model experiment by Katayama et al[8]. The formula is a function of the length and breadth of the flooded compartment and its water depth, the motion frequency and the roll amplitude.

For Case 3 with reduced GM, the static heeling arm due to accumulated water is calculated using normal hydrostatics. The freeing ports are assumed to be closed and the flow of water is considered only over the bulwark.

The numerical simulation model is extended to take account of the above roll damping effect and the heel moment effect of the WOD and then applied to the experiment cases. The results are shown in Fig 3. Here, the amount of water on deck, which was not measured in the experiments, is systematically changed for realizing reasonably good agreements in the numerical simulation. The results shown in Fig 3 indicate the reasonably good

agreements between the experiment and the simulation can be realized within the feasible range of the water amount on deck. The roll amplitudes in the numerical simulation for Case 2 and 3 are reduced because of roll damping effect due to water on deck. Here, the used water depth on deck is around 0.3m while the bulwark height is 2.7m. The mean roll angle in the simulation for Case 3 with reduced GM increases because of hydrostatic heeling moment due to water on deck. Here, the used water depth on deck is 0.5m while the bulwark height is 2.7m. The mutual importance of these two different effects of WOD could depend on the magnitude of hull restoring moment.
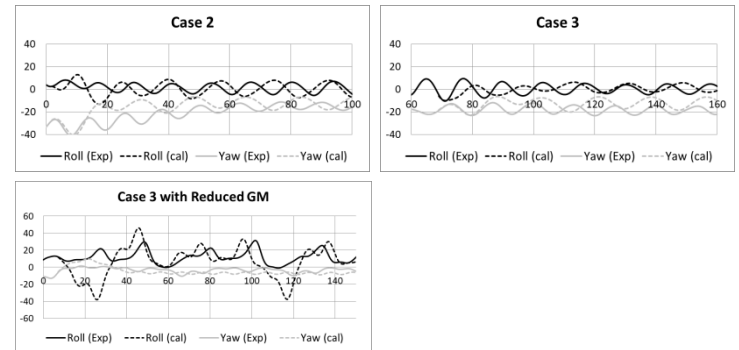
Fig. 3   Time series of simulation with WOD for regular waves of λ/L=1.5 and H/λ=0.1. Here, the Froude number is 0.29 for Case 2 and Case 3 and 0.15 for Case 3 with reduced GM.

4. Conclusions

It is confirmed experimentally that the Pure Loss Level 2 Criteria cannot be applied to ships with low weather deck length which is greater than 0.4Lpp and which is not completely surrounded by bulwarks.

The presence of WOD is important for the stability of the OSV. For high metacentric height, the presence of WOD reduces the roll oscillation. In contrast, when GM is reduced, the heeling moment due to accumulated water becomes more relevant.

References

1) Dillingham, J: Marine Technology, Vol.18, No.1, 1981.
2) Falzarano, J.M., Laranjinha, M., Soares, C.G.: ISSW, 2002.
3) Umeda, N., Aqmil, A. et al: ISSW, 2016.
4) Kubo, H., Umeda, N. et al: Proceedings of APHydro, 2012.
5) Hirano, M., Takashima, J.: Transactions of the West-Japan Society of Naval Architects, Vol.59, 1979.
6) Umeda, N., Yamakoshi, Y. et al: Proceedings of Sevastianov Symposium, 1995.
7) ITTC : Recommended Procedures, Numerical Estimation of Roll Damping, 7.5-02-07-04.5, 2011
8) Katayama, T.: Journal of JASNAOE, 2009.

A Study on Socio-spatial Structure of Informal Settlements by Analyzing Relationships between Physical Environment and Human Behaviors in the Inner-city Kampung, Jakarta.

Nugroho Sumanto

3rd Laboratory, Department of Architectural Engineering

Key Words: *Urbanization, Kampong, Socio-spatial structure, Physical Environment, Human behaviors.*

1. Introduction

Indonesia, in similar vein as other countries within the Southeast Asian region, is experiencing rapid urbanization and urban growth. Within the Indonesian Archipelago, more than half of the population (around 52%) resides in urban areas, a figure estimated to rise to 57.2 percent in 2020 (UN-Habitat, 2015). This trend is more pronounced in the Jakarta urban region, currently a mega city with more than 10 million inhabitants. With an urban population growth rate of 3.7 percent, the city is experiencing immense interurban and rural-migrant migration without significant supply in affordable housing and basic infrastructure facilities for most of its urban population.

The effect of this, has been the predominant distribution of kampong in Jakarta. Kampong, which refers to a settlement in rural surroundings that comes into being within urban conglomerations (Budiarto, 2003), is usually defined by characteristics such as poor either planning or housing conditions, and lack of basic infrastructure such as drainage, water, and sanitation. Even though these areas are marginalized and faced the threat of eviction, they have also provided a cheap housing solution and livelihood for many urban residents (low-income earners) since the Dutch colonial period. There have been several attempts to address the challenge of kampong include the KIP (1960s), public and private housing interventions and most recently million houses national program. Yet, the challenge of kampong persists without sustainable solutions that works for the urban poor.

This study, situated within the context of the above-mentioned challenges seeks to contribute to efforts in improving kampong through spatial analysis and bottom-up settlement improvement strategies. The first step, this study argues, is to obtain a better understanding in the existing socio-spatial structure of kampong within Jakarta, in terms of spatial and behavioral aspects to inform better planning, design and policy strategies.

The objective of the study was therefore (i) to analyze the existing spatial structure of kampong, (ii) to understand relationship between human behaviors and informal open space. Kebon Kacang, which is one of the inner-city kampongs within the Central Business District (CBD) of Jakarta was selected as the case study area. It is located centrally within the Tanah Abang subdistrict, Central Jakarta. This area is surrounded by the city's most important and prestigious commercial, business and service areas such as Plaza Indonesia Shopping Mall, Grand Hyatt Hotel, the Japanese Embassy, and the UN local headquarters.

Research methodology adopted for the study included house-to-house field survey in two different communities: RW3 and RW8 of Kebon Kacang (see Fig. 1). The process included literature review, field observation, questionnaire based interviews with 110 heads of households (35 from RW3 and 75 from RW8) and institutional interviews, and mapping of human behavior. Since the two community are divided into neighborhood units, five houses were randomly selected in all the neighborhood units. In each house, the head of household was selected for the interview. For the purposes of understanding human behavior, open spaces were selected and human behaviors (activity, age, time and gender) were directly observed and mapped.

Fig. 1 Map of studied areas in Kebon Kacang, Central Jakarta.

2. Findings

The findings from this field survey, using the methodology described above, are presented below.

In terms of land tenure, the survey revealed that main mode of land acquisition was family inheritance. However, land status, which refers to the right to use land, was 'Hak Girik' (Land Tribal Right): a Dutch colonial era practice which granted holding title to residents for cultivation. However, it appears residents over the years have interpreted holding right as 'building and use right', leading individual house construction and claim of land and property ownership.

The study also identified several evidences of house modification among residents in the study areas. In both of the study areas, house modifications included parts of the house such as roof, walls, floors or extension of number of rooms. Change in function of rooms, for example conversion of living rooms into bedrooms for rental purposes. They are several reasons behind these practices, including improving house condition after disaster (e.g. fire or flooding) or generating income from rent to improve house conditions. However, owners were more likely to modify the house than tenants.

Another important finding was the significance in location in determining access to facilities and services such as water and

sanitation. The field survey revealed houses located along local access roads were better served with facilities such as water whereas those around cul-de-sacs were poorly served. This is due to the cost of extending services to inner parts of the study communities, according to interviews. Additionally, even though both toilet and bathroom facilities were available in the study areas, there was no septic tank. Consequently, one-fifth of the residents' deposit waste water into gutters. This is a major problem for choked gutters, which cause flooding problems during heavy rains.

Informal economic activity remains the dominant sector in terms of labor and employment in the study areas. In both RW3 and RW8, the main activities included food vending, tailoring, motorcycle drivers, and kiosk-style grocery stores. In RW8, which is closer to the CBD, most of the residents engaged in mobile food vending, street markets, tailoring and many others. The reason behind this was the concentration of commercial activities and population around the CBD provided customer base for those involved in informal economic activities.

In term of spatial network, the study categorized a 5-level hierarchy based on function. The typology of the spatial networks is categorized into four groups based on an order of openness: I, U, T, and Z. Thus, I and U are more open (linking the studied areas externally to other parts of the sub-district) and had wider width (not less than 2.5 meters) while T and Z, are typically irregular, spontaneous and connecting houses and isolated spaces (width less than 2.5 meters).

In view of human behavior in informal open spaces, the study revealed a relationship between the typology of open space and the category of human behavior. This was also influenced by the openness of the different typology of the spatial networks. For instance, I type, in both RW3 and RW8 more economic oriented behaviors such as street vending, mobile food vending, kiosk-style shops (see Fig. 2). The reason for this is due to the openness of the I typology. Also, social activities such as chatting, gathering and lingering were observed around the spots where economic activities were organized. For T type, the study observed more social and stationary activities such as chatting, gathering, sitting or lingering. The Z, which is less open in comparison with I and T, had no significant activities—passive space. This is because of the narrowness (less than 1.2 meters) its connection with other open spaces is limited.

Generally, open spaces that had seating facilities, trees or tents had more social activities since it provided comfortable situation for residents. The study also revealed that the presence of free Wi-Fi in open spaces affected the social human behavior as more young people gathered to use internet and chat. Residents have also

introduced speed bumps on some roads to reduce motor traffic and encourage children to play on these roads.

3. Conclusions

Jakarta's dual city status, in terms of daily intersections of formal and informal socio-spatial and economic aspects, exert significant implications on the urban planning and design of this mega city. The study has attempted to provide a field based analysis of an inner-city kampong, at the heart of the Jakarta. The aim has been to comprehend the socio-spatial aspects of existing conditions and human behavior aspects of open spaces.

This thesis has contributed to locally based understanding of kampong in Indonesia. The study has affirmed the findings in previous studies about Kampong (and informal settlements generally), such as the residents' occasional housing modification to deal with declining physical conditions, and to take advantage of income opportunities (rent or commerce). Additionally, how the spatial structure, openness and typology of open spaces directly influence human behaviors such as gathering, chatting, selling or even sitting.

Based on the findings from the study, a couple of recommendations have been made to improve current conditions. Firstly, improve the condition of open spaces to enhance their usability and comfortably for residents, especially children. Secondly, redesign the spatial networks of roads and alleys to improve accessibility, social liveliness, and the opportunity for residents to continue informal economic activities such as food vending. In terms of community planning, supporting residents to organize (through bottom-up processes) and initiate interventions in their neighborhoods (participatory community planning and development).

Future research could take into consideration comparative socio-spatial analysis of different kampong to identify potentials, positive aspects and model for improvement.

References

1) Budiarto, L. Dwellers and strangers: Socio-cultural entity, space-use, and spatial configuration in kampung settlement of Jakarta, Indonesia. Proceedings of the 4th International Space Syntax Symposium, London. 2003.
2) The State of Asian and Pacific Cities. Urban transformations: Shifting from quantity to quality. United Nations Commission for Human settlements, UN Habitat. Nairobi: Kenya 2015.

Fig. 2 Observed human behavior in the inner-city kampong in Kebon Kacang, Central Jakarta, Indonesia.

Flow Field Measurement Around Self-Propelled KRISO Container Ship Model in Head Waves

Htike Aung Kyaw

Hull Form Design Sub-Area, Department of Naval Architecture and Ocean Engineering

Key Words: *KRISO Container Ship (KCS), Particle Image Velocimetry (PIV), EFD, Flow Field Measurement, Head Waves*

1. Introduction

During designing process of a ship, one of the main and most common problems which the Naval Architects face is the necessity to ensure that the combination of hull form and the propulsion arrangements are at the most efficient state in sense of hydrodynamics and within the design requirements. The most important task would be that the ship shall perform at the designated speed with the minimum power while having the highest propulsive efficiency without endangering the ship and its crew in any circumstances. Generally speaking, this can be achieved only by proper matching of the hull and the propeller. Thus, Propeller-Hull interaction is a conspicuous topic in designing a sustainable ship. Another issue worth mentioning would be the global warming. Reduction of greenhouse gas emissions is underway around the world so as to prevent global warming. The performance of propulsion of ships in waves is important for reduction of CO_2 emission in actual voyages.

Studies are being made on fluctuations of the inflow velocity to propeller and change of velocities before and after the propellers and rudders in a way to develop feasible energy saving devices and achieve higher propeller efficiencies. CFD (Computational Fluid Dynamics) is also rapidly improving nowadays and detailed simulation of flow field around ships in waves are also progressing very fast. Various CFD softwares are being developed and widely used in research, development and design steps. However, the detailed measurement data around ships in waves are not yet enough to validate the accuracies of the CFD.

Here, the flow field is measured in waves using a stereo PIV (Particle Image Velocimetry) at the downstream section of the rudder of a self-propelled KCS ship model. Self-propulsion experiments in waves have been conducted and the test conditions for this PIV measurement had been determined.

2. Outline of Experiment

2.1 Overview of Experiment

A 3.2 m KRISO Container Ship (KCS) model has been used for this experiment. Various experiments were conducted in the towing tank of Osaka University by our team. This experiment was conducted to measure the flow field at the downstream section of the rudder using the PIV systems for the self-propelled ship model in head waves. Principal Particulars of the model are as shown in Table.1. A 5-blade propeller was installed at a position 56mm forward of AP. This propeller has a diameter of 0.1099m, pitch ratio (P/D) of 0.95, expended area ratio (A_E/A_O) of 0.8002 and a hub ratio of 0.18. Open-Water Test had been conducted for this propeller beforehand. PIV experiment for flow field measurement was conducted in mid-April where average air

temperature was about 16°C and average water temperature was around 13°C.

Table 1 Principal Particulars of KCS Model Used.

Length (B.P)	L_{BP} (m)	3.200
Breadth	B (m)	0.448
Depth	D (m)	0.264
Draft	T (m)	0.150
Displaced Volume	∇ (m³)	0.140

Fig. 1 KCS Model in Towing Tank.

2.2 Experimental Conditions

Pitch and roll free gimbal under the load cell attached on the bottom end of the heaving rod was mounted at the center of gravity the model and this heaving rod was installed in a light weight carriage. A servo-type wave meter was installed 3.24 m in front of FP, to acquire incident wave data. The ship was free to surge, heave and pitch. Motor and dynamometer were installed for self-propulsion tests. Forces on longitudinal (x)-direction (F_x) were measured using a load cell attached to the heaving rod where positive F_x was taken towards the aft of the ship. Wave elevation, F_x, heave, pitch, surge, thrust and torque were measured and logged for each experiment condition. From this, we could plot a times series data of aforementioned data and calculate terms such as effective inflow velocity, surge velocity, surge acceleration, hydrodynamic force etc. as shown in Fig. 2.
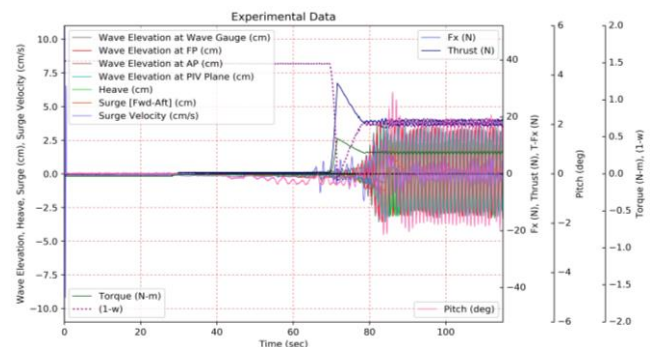

Fig. 2 Time Series of Logged and Calculated Data for $\lambda/L_{BP} = 1.15$.

3. Stereoscopic PIV Measurements in Waves

PIV Measurements were made for head waves of $\lambda/L_{BP} = 0.65$, 1.15 and 1.37 with the ship speed of 1.456 m/sec, i.e. Froude Number 0.26. The PIV measurement plane is located at 80 mm aft of AP. PIV laser and cameras were triggered by delaying the calculated time period for each wave condition using the zero-crossing signals from the wave meter.

In this PIV measurement, the flow field at a plane behind the rudders was measured around the self-propelled ship model in waves. In Fig. 3, the velocity distribution is shown for wave condition ($\lambda/L_{BP} = 1.15$). The zero degree phase shown here is the moment when average value of the wave elevation at wave meter changes from minus to plus. The other phases are shifted every ¼ period. The flow velocity and the coordinates shown here are non-dimensional. For each λ/L_{BP}, PIV images were taken at 3 different water depths to ensure the coverage of the whole flow field for each wave condition and to overcome the vertical limits of the PIV system. The number of data used for time averaging of each depth was about 100 images per phase.
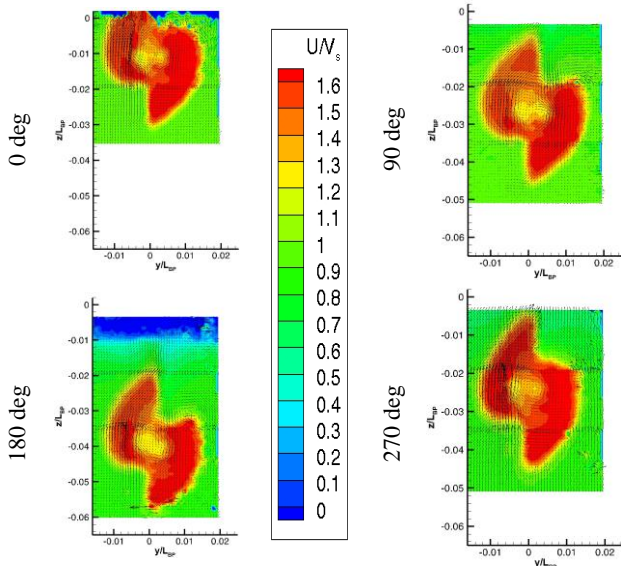

Fig. 3 Phase-Averaged Velocity Distribution in Waves.

4. Comparisons

This experiment focused mainly on flow field measurement at aft of rudder for a self-propelled KCS model in head waves but it is not just limited to visualizing the flow field at the point of interest. Comparisons of the ship motions corresponding to waves with other tests facilities were carried out so that the accuracy of the experiment itself can be confirmed. Not to mention, we also compared the trend of graphs for thrust and torque, resistance and powering as well as the propeller revolutions for calm water and each wave conditions with the data received from FORCE Technology. FORCE Technology used a 6.0702 m KCS model and conducted with Heave and Pitch being free. During our experiment, 3 DOF (degree of freedom) ship motion was considered, namely, heave, pitch and surge using a weak spring arrangement whilst keeping the ship in an average position with regards to the towing carriage.

Furthermore, non-dimensionalized wave elevation, heave and pitch with FORCE Technology's model and Iowa Institute of Hydraulic Research (IIHR)'s free-running 2.7 m model data have been compared. The results of comparisons were found acceptable as in Fig.4 graphs.
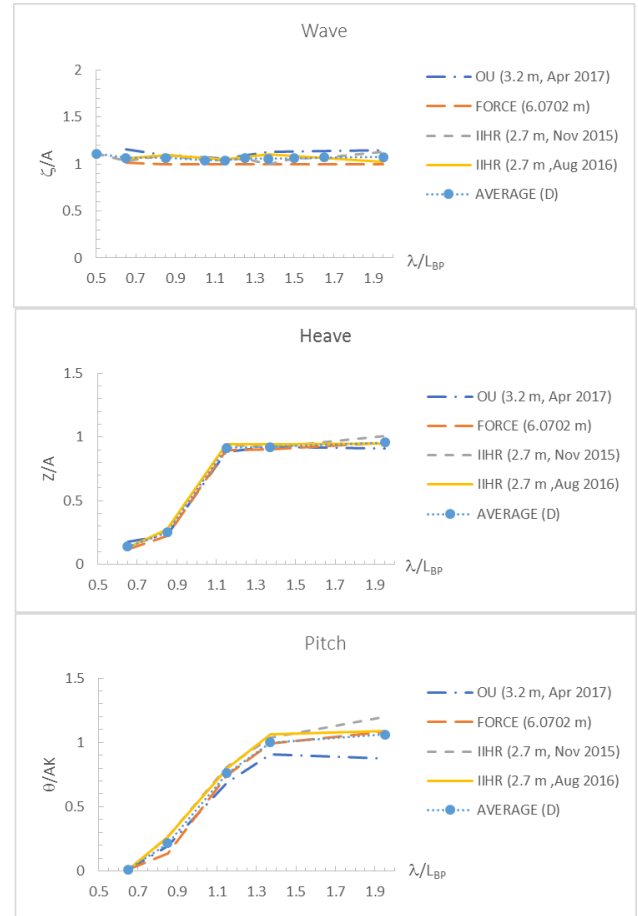

Fig. 4 Comparison of non-dimensionalized wave and ship motions among other institutions.

5. Conclusions

Ship motions such as heave and pitch had been confirmed with various test facilities and were found agreeable although the test methods in each facilities were different: FORCE Technology having only 2 DOF, IIHR conducting as free-running model.

More accurate flow field measurements can be done using the PIV systems if the number of runs increases so as to obtain more images or if PIV system can have larger vertical field of view so that we could run less number of vertical depths whilst having more images for the same number of test runs.

Flow-field calculated by CFD for the self-propelled KCS in head wave conditions will be conducted in the future. With the experimental data and flow-field measurement provided by the present work, CFD result will be validated and modified to explain the phenomena in this experiment.

References

1) Tamaki, K (2017): Study on Fluctuating Flow Field around Container Ship Stern in Waves, Osaka University.
2) FORCE Technology, Claus D. Simonsen (2017): Added Powering in Regular Head Seas.
3) IIHR Test Summary: T2015 Case (Updated: February 2017)

Numerical Study on Determination Technique for Equivalent Distributed Stress

Ahmad Zakky

Ocean Material Engineering, Department of Naval Architecture and Ocean Engineering

Key Words: *Equivalent distributed stress, Crack cohesive force model, Crack opening displacement, Stress intensity factor, Finite element method*

1. Introduction

In this study, a new EDS determination method based on left opening right closing integral capable of avoiding the singularity[1] is proposed. In this method, EDS is approximated by 3rd order spline interpolation without singularity. When EDS's spline knots are arranged at SIF's evaluation positions in the a-K relation, the spline coefficients are determined by using the SIF at a point nearby to notch bottom. When the spline knots are arranged irrelevantly to the *a-K* relation, the coefficients are determined by least square method (LSM). The validity of proposed methods are examined by comparing the estimated fracture mechanics parameters (SIF and COD) with those derived from the strict solution or elastic-plastic finite element (EPFE) analyses.

2. New approach for the EDS evaluation

The EDS for an ICC panel subject to uniform remote loading (Dugdale model) should be uniform and equal to the remote stress. Let us consider an ICC panel with a crack half-length of *c*. The position on the crack face is specified by the *x*-coordinates in Fig.1. Let N_ξ be the number of division for spline interpolation, $\xi_i (i=1,\ldots, N_\xi)$ *x*-coordinates of the right end for the *i*-th division section, and $\xi_0 = x_0$ at the notch bottom($a=0$). EDS in the *i*-th section $f_i(x)$ is approximated by 3rd order spline interpolation by the equation below:

$$f_i(x) = \alpha_i x^3 + \beta_i x^2 + \gamma_i x + \delta_i \quad (\xi_{i-1} < x \le \xi_i); i = 1,\ldots,N_\xi \tag{1}$$

where, α_i, β_i, γ_i, δ_i are cubic spline interpolation coefficients. $\{\xi_i (i=0,\ldots,N_\xi)\}$ are spline knots. Let N_a be the number of SIF evaluation point, and a_j ($j=1\ldots Na$) be the x-coordinates of the *j*-th evaluation point. N_a is chosen so that $N_a \ge N_\xi$. Let K_j be the SIF at $x=a_j$. Superposition principle leads to the equation of K_j below:

$$K_j = \frac{2}{\sqrt{\pi a_j}} \sum_{i=1}^{a_j \le \xi_i} \int_{x=\xi_{i-1}}^{\min(a_i,\xi_i)} \frac{f_i(x)}{\sqrt{1-(x/a_j)^2}} dx ; \ j = 1,\ldots,N_a \tag{2}$$

where, $f_i(x)$ is given by Eq. (1).

The spline's continuum conditions at knots for 0th-2nd derivatives and the natural spline's endpoint conditions are given. Then this conditions are the governing equations that relate the spline coefficients to the requirements of spline EDS model (*a-K* relation, spline's continuum conditions and natural spline's conditions). Let *m* be the number of governing equations and *n* the number of spline coefficients. The *m* and *n* are given by equations below:

$$m = N_a + 3(N_\xi - 1) + 2, \quad n = 4N_a \tag{3}$$

When the spline knots are arranged irrelevantly to the *a-K* relation and $N_\xi \ll N_a$, *m* becomes larger than *n*. The governing equations can be written as Eq. (4). This system of linear equations is over determined, and the spline coefficients can be determined by linear least square method. In this case, the *a-K* relation is not strictly established, but EDS's spatial instability can be suppressed.

$$[A]\{U\} = \begin{bmatrix} A_{11} & \cdots & A_{1n} \\ \vdots & & \vdots \\ \vdots & & \vdots \\ \vdots & & \vdots \\ \vdots & & \vdots \\ \vdots & & \vdots \\ \vdots & & \vdots \\ A_{m1} & \cdots & A_{mn} \end{bmatrix} \begin{Bmatrix} \alpha_1 \\ \beta_1 \\ \gamma_1 \\ \delta_1 \\ \vdots \\ \delta_{N_\xi} \end{Bmatrix} = \{RHS\} = \begin{Bmatrix} K_1 \\ K_2 \\ \vdots \\ K_{N_a} \\ 0 \\ \vdots \\ 0 \\ 0 \\ 0 \end{Bmatrix} \tag{4}$$

When spline knots are arranged at SIF evaluation positions in the *a-K* relation, $N_\xi = N_a$, and $m = n-1$. This makes the system Eq. (4) to be underdetermined, and there is no unique solution. In this case, the equation of the SIF at a point nearby to notch bottom, shown below, is appended to the governing Eq. (5).

$$K_{sx_1} = \frac{2}{\sqrt{\pi(sx_1)}} \int_{x=x_0}^{sx_1} \frac{f_1(x)}{\sqrt{1-(x/(sx_1))^2}} dx \tag{5}$$

where, K_{sx1} is the SIF at $x = sx_1$ ($0 < s < 1$). This point nearby to notch bottom is within the 1st (the closest to the notch bottom) spline section, and the right hand side of Eq. (5) becomes a linear equation of $\{\alpha_1, \beta_1, \gamma_1, \delta_1\}$. In this case, $n = m = 4N_a$, and the governing equations can be written as:

$$[A']\{U\} = \begin{bmatrix} A'_{11} & \cdots & A'_{1n} \\ \vdots & & \vdots \\ A'_{n1} & \cdots & A'_{nn} \end{bmatrix} \begin{Bmatrix} \alpha_1 \\ \beta_1 \\ \gamma_1 \\ \delta_1 \\ \vdots \\ \delta_{N_\xi} \end{Bmatrix} = \{RHS\} = \begin{Bmatrix} K_1 \\ K_2 \\ \vdots \\ K_{N_a} \\ 0 \\ \vdots \\ 0 \\ 0 \\ 0 \end{Bmatrix}. \tag{6}$$

This system of linear equations is a full-rank system, and the solution is unique. In this case, the *a-K* relation is strictly established, but the system becomes ill-conditioned, and EDS's spatial instability due to over fitting may occur. Hereafter, the point at x=sx1 is called 'NBP (nearby point)'. Hereafter, EDS

determination in which spline knots are arranged at SIF evaluation points and utilize the SIF at NBP is called 'NBP' determination.

For LSM determination, the approximated solution of Eq. (6) can be calculated by adopting least square method (LSM) as shown below:

$$\{U\} = \left[A^+ \right]\{RHS\}; \left[A^+ \right] = \left([A]^T [A] \right)^{-1} [A]^T \tag{7}$$

where, A^+ is the Moore-Penrose pseudo inverse. The strict solution of Eq. (4) is calculated by solving the linear equation system.

3. Development of strip yield model based on EDS

From a-K relationship subject to an external load and that subject to a uniform cohesive stress equivalent to yield stress, Crack opening displacement (COD) derived from each stress can be calculated, then, COD in strip yield model is obtained as follow,

$$V(b) = V^P(b) - \lambda \sigma_Y V^Y(b) \tag{8}$$

where, $V^P(b)$ is COD derived from an external load, and $V^Y(b)$ is COD derived from cohesive stress. λ is plastic constraint factor, σ_Y is yield stress.

4. Numerical example

In order to examine the applicability of proposed EDS determination techniques, FM parameters of a semi-circular surface crack in an out-of-gusset welded joint studied by Kajimoto[2], are calculated by EDS-based crack cohesive force (CCF) model. The crack depth is 5 mm and external force 100 MPa is applied. σ_Y is 392 MPa. Young's modules is 20,600 MPa, and Poisson's ratio is 0.3. a-K relations are prepared by performing linear finite element FCP (LFEFCP) analysis, and the reference solutions of EPFM parameters (COD and γ_p) are calculated by performing elastic-plastic finite element (EPFE) fracture mechanics analyses.

As the result in Fig. 2 shows the comparison of f_P determined by the proposed EDS determination techniques. This figure shows that a large numerical instability appears near the notch bottom (c<0.5mm) (3D_NBP). f_P becomes negative at the notch bottom. This cannot be logical, and FM parameters calculation based on this EDS is meaningless. It is considered that this is due to the extremely large amount of unbalance in segment length, and the poor accuracy of the SIF at NBP estimated by the extrapolation. Fig. 10 shows that this numerical instability is well suppressed in cases 3D_LSM0.5 and 3D_LSM0.25, and the f_P's stability becomes better with the increase in spline segment length.

Fig. 11 also shows that the EPFE's COD (V_{FE}) approximately agrees with CCF model's CODs when a finite quantity of V_{FE} is calculated. On the real crack face (c<5mm), the COD for case 3D_NBP shows a strange decline in the 1st spline segment (c < 0.205mm, adjacent to the notch bottom), while those for LSM cases it shows smooth and monotonic changes. It is considered that the strange COD in case 3D_NBP is due to the EDS's numerical instability (Fig. 10). The difference in CODs for LSM cases is negligibly small when the spline knots interval is larger than 0.25. These results show that it is essential to adopt LSM-based EDS determination technique for the cases without highly precise SIF for infinitely small cracks, and there is no

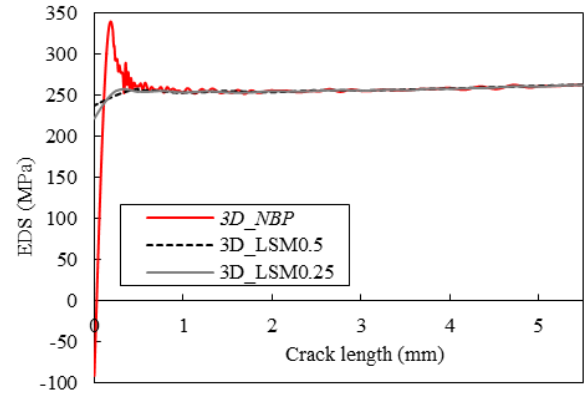needed to adopt spline knots intervals smaller than 0.5mm under conditions chosen.

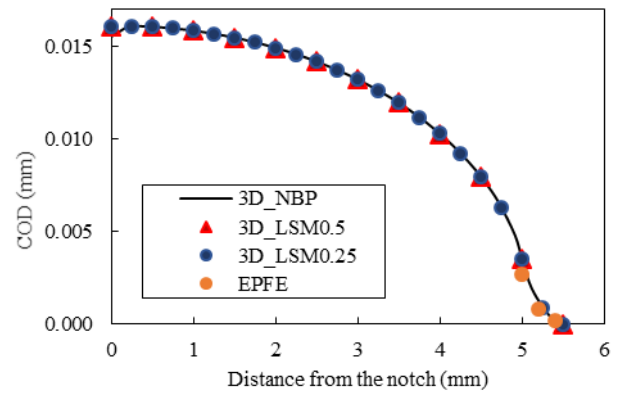Fig.1 The comparison of EDS's of an out-of-gusset welded joint

Fig.2 The comparison of COD's of an out-of-gusset welded joint

5. Conclusions

In this study, an EDS determination method based on left opening right closing integral capable of avoiding EDS's singularity has been proposed with high prediction accuracy to estimate various elastic-plastic FM parameters for infinite center cracked panels. This demonstrates the effectiveness of the FM parameter calculation techniques based on a left opening right closing integral, which is capable of avoiding EDS's singularity. It is essential to adopt LSM-based EDS determination technique for the cases without highly precise SIF for infinitely small cracks (such as a surface crack in a three-dimensional welded joint), and there is no needed to adopt spline knots intervals smaller than 0.5mm under conditions chosen. In other hand, it is needed to examine the plastic constraint factor λ, which is used in CCF-model analysis, for various three-dimensional cracks by performing EPFE and crack cohesive force (CCF) analyses.

References

1) Osawa Naoki et.al.: Papers on Japan Maritime Ocean Engineering Lecture, 2015 A - GS 8 – 3
2) Kajimoto Katsuya: Doctoral thesis, Hiroshima University, 1985.